Full length article

Amorphous-to-crystal transition in the layer-by-layer growth of bivalve shell prisms

Julien Duboisset[a], Patrick Ferrand[a], Arthur Baroni[a], Tilman A. Grünewald[a],
Hamadou Dicko[a], Olivier Grauby[b], Jeremie Vidal-Dupiol[c], Denis Saulnier[d],
Le Moullac Gilles[d], Martin Rosenthal[e], Manfred Burghammer[e], Julius Nouet[f],
Corinne Chevallard[g], Alain Baronnet[b], Virginie Chamard[a,*]

[a] Aix-Marseille Univ, CNRS, Centrale Marseille, Institut Fresnel, Marseille, France
[b] Aix-Marseille Univ, CNRS, CINaM, Campus Luminy, Case 913, 13288-Marseille cedex 9, France
[c] IHPE, Univ. Montpellier, CNRS, Ifremer, Univ. Perpignan Via Domitia, Montpellier France
[d] Ifremer, UMR 241 Environnement Insulaire Océanien (EIO), Labex Corail, Centre du Pacifique, BP 49, Vairao 98719, French Polynesia
[e] European Synchrotron Radiation Facility, F-38043 Grenoble Cedex, France
[f] GEOPS, Univ. Paris-Sud, CNRS, Université Paris-Saclay, 91405 Orsay, France
[g] NIMBE, CEA, CNRS, Université Paris-Saclay, CEA Saclay 91191 Gif-sur-Yvette Cedex, France

ARTICLE INFO

ABSTRACT

Biomineralization integrates complex physical and chemical processes bio-controlled by the living organisms through ionic concentration regulation and organic molecules production. It allows tuning the structural, optical and mechanical properties of hard tissues during ambient-condition crystallisation, motivating a deeper understanding of the underlying processes. By combining state-of-the-art optical and X-ray microscopy methods, we investigated early-mineralized calcareous units from two bivalve species, *Pinctada margaritifera* and *Pinna nobilis*, revealing chemical and crystallographic structural insights. In these calcite units, we observed ring-like structural features correlated with a lack of calcite and an increase of amorphous calcium carbonate and proteins contents. The rings also correspond to a larger crystalline disorder and a larger strain level. Based on these observations, we propose a temporal biomineralization cycle, initiated by the production of an amorphous precursor layer, which further crystallizes with a transition front progressing radially from the unit centre, while the organics are expelled towards the prism edge. Simultaneously, along the shell thickness, the growth occurs following a layer-by-layer mode. These findings open biomimetic perspectives for the design of refined crystalline materials.

Statement of significance

Calcareous biominerals are amongst the most present forms of biominerals. They exhibit astonishing structural, optical and mechanical properties while being formed at ambient synthesis conditions from ubiquitous ions, motivating the deep understanding of biomineralization. Here, we unveil the first formation steps involved in the biomineralization cycle of prismatic units of two bivalve species by applying a new multi-modal non-destructive characterization approach, sensitive to chemical and crystalline properties. The observations of structural features in mineralized units of different ages allowed the derivation of a temporal sequence for prism biomineralization, involving an amorphous precursor, a radial crystallisation front and a layer-by-layer sequence. Beyond these chemical and physical findings, the herein introduced multi-modal approach is highly relevant to other biominerals and bio-inspired studies.

1. Introduction

Biomineralization integrates complex biological, chemical and physical processes to control the formation and structuring of mineralized tissues in living organisms [1,2]. The versatility of the

* Corresponding author.
E-mail address: virginie.chamard@fresnel.fr (V. Chamard).

biomineralization processes is remarkably illustrated by their capability to often simultaneously produce different crystalline polymorphs under the same external conditions, presenting morphological site- and species-specific architectures [3,4]. The consistent presence of a sub-micrometric granular structure, [5,6] as observed in many marine shell calcareous carbonates, silica sponges, carbonated hydroxyapatite of bone and tooth enamel, [6] and even in fossil marine biominerals as old as the Ediacaran (550 Ma) [7] points towards some mechanism generics in the mineralization process. Deciphering these mechanisms is of crucial importance: besides the fundamental challenges crystallisation under biological mediation represents, it will provide bio-inspired strategies for the synthesis of nanostructured inorganic materials using *e.g.*, green chemistry approaches [8]. Despite extensive studies, the complexity of the biomineralization processes is continuously highlighted [2], evidencing that classical crystallisation theory can not be invoked to explain the formation of most of organo-mineral crystals and thus, that a detailed understanding of biomineralization is still lacking to date.

Calcium carbonate mollusc shells and echinoderms, which raise interest owing to their hierarchically organized structures, are often used as model systems [9]. In particular, while bivalve molluscs shells often present a complex 3D architecture, *Pinctada margaritifera (Pm)* and *Pinna nobilis (Pn)* represent simpler models. The shells of *Pm* and *Pn* are organized in two mineralized layers composed of crystalline biomineral units (*i.e.*, an external layer of elongated calcite prisms [10–12] and an internal layer of aragonite nacreous tablets [13,14]), produced simultaneously and extra cellularly by the organism [4]. The whole structure is lined by an organic membrane, the periostracum, covering the outer shell. An organic envelope individually surrounds prisms and nacre tablets [4]. These species are model systems commonly used [15,16] to study the biological, chemical and physical processes at play during biomineralization due to their comparatively simple shell architecture. Knowledge on the composition of the organic matrix, produced by the organism, holds the promise to understand at which structural level the biological control over the biomineralization process is exerted [17–19]. With the advent of proteomics, tremendous progress has been made in the identification of the proteins contained in the mollusc organic matrix [20], showing that the majority of these proteins are specifically associated to the production of either calcite prisms or aragonite nacreous tablets. However, knowledge of the precise function of these proteins (and other sugars and lipids) remains elusive and is mostly based on *in vitro* crystallisation assays [21–24] and microscopy investigation of labelled biominerals [25–27]. The presence of intra-crystalline organic molecules is as well reported [25–27] and confirmed by transmission electron microscopy [28]. In addition to the question of the role of the different organic molecules, the specific crystallisation pathways, *i.e.,* the different mechanisms by which the initial ions associate to build the final granular crystals [7] are also under debate [29]. In sea urchins [30–32], corals [33,34] and molluscs [35–37], the repeated observation of amorphous calcium carbonate, an otherwise metastable $CaCO_3$ polymorph, leads to consider it as transient precursor of the crystallisation pathway [38], which could be temporarily stabilized by factors such as granules of finite size [39,40], by the presence of organic macromolecules [41] and/or by the mantle cells [42]. These observations provide guidelines for formulating biomineral growth models, as already proposed for sea urchin spine [43], the nacreous layer [27,28] and the prismatic layer [16,26,44].

The ideal strategy to study the biomineralization processes, the *in vivo* investigation of the crystallising organisms, is however as appealing in theory as it is challenging in practice [45]. This practical difficulty can be partly circumvented by the investigation of biomineralized units in their early growth stages

[44,46], allowing one to, at least partially, infer a temporal sequence of the biomineralization mechanisms. While the observation of post-mortem biominerals only gives access to stable post-crystallisation stages and not to the transient stages occurring during the biomineralization process, the presence of developing biomineralized units in their early growth stages is susceptible to provide decisive pieces of information, allowing one to bridge those gaps. We devise this strategy in this article, thanks to the use of highly-resolved, highly-sensitive experimental approaches, which are able to probe the early biomineralized units in their pristine state, with negligible impacts of radiation-induced damage. In particular, we take advantage of two recently developed optical microscopy methods, coherent Raman scattering [47] and vectorial ptychography [48,49], applied for the first time to the biomineralization problem, in order to provide chemical and crystalline (via the optical properties of the crystal) structural information, respectively. Those approaches are complemented by state-of-the-art, highly resolved X-ray diffraction microscopy method. In this way, we are able to assemble a very detailed picture of the early-mineralized prism units of *P. margaritifera* and *P. nobilis* shells. While these two selected species present well-documented differences in their prismatic structure (*e.g.*, crystalline orientation distribution [50], organic composition, *etc.*), they both produce single-crystalline calcite prisms at the shell growth edge [4]. While the presence of morphological rings decorating the external side of the prisms is interpreted as a first radial growth stage [14,16], the repeated observations of layered structures along the prism growth direction, of both morphological [51] and chemical [52] nature, points towards a sequential layer-by-layer growth model [53].

In this work, we further report for both species, the presence of ring-like chemical and crystalline structures within these units, corresponding to amorphous calcium carbonate- and organic-rich regions, also associated with a modification of the crystalline order and strain. Those findings, put into the context of a biomineralization sequence, are pointing towards a radial crystallisation front, arising from the transformation of an amorphous calcium carbonate precursor, most likely in a cyclical manner, creating subsequent layers. We hypothesize that the role of the organics likely involves the stabilization of the amorphous precursor, the spatial registration, and strain and optical property mediation.

2. Materials and methods

2.1. Sample preparation

The juvenile *Pinctada margaritifera* shells were farmed at the IFREMER hatchery at the biological station of Vairao (Tahiti). They were cultivated in an optimal and sanitary-controlled environment to avoid any contamination during growth. Once selected, they were preserved in a 70% ethanol/water solution and transferred to the Institut Fresnel in Marseille (France).

The *Pinna nobilis* shell pieces were sampled in 10/2013 and came from specimen living in the Mediterranean Sea (Giens, France). No animal was captured or killed. Small, millimetre-sized pieces were removed *in situ* from the spines covering the outer shell, in the vicinity of the shell growth margin and further preserved in a 70% ethanol/water solution.

2.2. Coherent Raman scattering microscopy

Two optical micro-spectroscopy techniques were used to image the structural distribution of calcium carbonate and organic molecules using the sensitivity of coherent Raman with respect to specific vibrational modes [47,54]: coherent anti-Stokes Raman

scattering (CARS) and stimulated Raman scattering (SRS). For both imaging modalities, the laser pulse duration of around 2 ps, transfers to 12 cm^{-1} spectral resolution [47]. The lateral and axial resolutions were measured to be 350 nm and 2.5 μm, respectively. For both modalities, the calcite symmetric-stretch C-O vibration value was calibrated with a calcite geologic crystal and found at 1085 cm^{-1}, as referenced [55]. A mode-locked laser (picoEmerald, APE, 80 MHz repetition rate) delivers synchronous pulses at two different wavelengths, one called Stokes at 1032 nm and one other tunable pulse within a range of 730–960 nm, called pump. The two beams overlap in time and space and are focused using a water immersion objective (40x, NA 1.15, CFI Apo Lambda S LWD, Nikon). The image acquisition is performed using galvanometric scanning mirrors (6200 H, Cambridge Technology). Typically, the pixel dwell time is 40 μs and the average powers at the focal spot are about 5–15 mW. The forward emitted light is collected in transmission using a long working distance in-air objective (40x, NA 0.6, LUC-PLFLN, Olympus) and focused on a channel photomultiplier tube (Hamamatsu, H10682). In the SRS mode, the experimental scheme is slightly modified. An Electro Optic Modulator (EOM) modulates the intensity of the Stokes beam at 20 MHz. The forward signal is focused on the detection module (APE SRS detection set), which comprises a large-area photodetector and a lock-in amplifier. The intensity of the modulated transfer from Stokes to pump is measured with an integration time of 100 ns. CARS and SRS modalities were alternatively used following the evolution of the set-up

For the *P. margaritifera* investigations, the shells were cut into pieces of about 1 mm^2 and placed onto a microscope coverslip in an ethanol/water solution. For the *P. nobilis* investigation, the sample was fixed on a tip and measured in air. For both experiments, the threshold of beam-induced damage has been determined on a different region on the sample and a power of about 50% of the threshold value was used to ensure negligible effects.

2.3. Optical vectorial ptychography

Measurements were carried out on a custom-built setup for optical vectorial ptychography [48], operating at a wavelength of 635 nm. The object was placed on a motorized stage (U-780 from Physik Instrumente) and scanned under a finite-sized probe with effective diameter of 100 μm, selected optically by placing a 2-mm diameter iris diaphragm in the image plane of a 20 × objective lens (ACHN-P, NA 0.4, Olympus). The camera (Stingray F-145B, Allied Vision, 320 × 240 effective pixels of 25.8 × 25.8 μm^2 after binning) was placed 190 mm downstream of the diaphragm. The acquisition time was set so that the whole camera 14-bit dynamical range was used. For *P. nobilis* and *P. margaritifera* shells, the scanning grid contained 459 and 270 points, respectively, with average steps, along the two scanning directions, of 11 μm and 9 μm, respectively. All scans included additional random step fluctuations of ±50%, in order to avoid periodic reconstruction artifacts. At each scanning position, three linearly polarized probes at angles of 0, 45, 90° in the object plane and three linear analyser orientations at angles of 0, 45, 90° were used, resulting in nine different combinations. Object reconstructions were performed by means of the conjugate gradient algorithm, allowing the joint estimation of the three illumination probes together with the complete optical properties of the object [56]. *P. nobilis* and *P. margaritifera* shell image reconstructions have been obtained after 950 and 500 iterations, respectively. In this study, we focus on the optical path length (OPL), the retardance (R) and the Eigenpolarization ellipticity (EPE) [49]. The transverse spatial resolution is approximately estimated to 0.8 μm.

2.4. X-ray microscopy

The X-ray nanoprobe Bragg diffraction experiments were performed at the ID13 beamline of the European Synchrotron Radiation Facility. The 14.64 keV monochromatic beam was focused down to the sample position using a set of crossed silicon refractive lenses of 25 μm effective aperture and 0.01 m focal length. This produces a beam size of 80 nm (FWHM) at the focal plane. The sample, fixed on a metallic tip was mounted onto a three-axis piezo-electric stage, itself placed on the top of a hexapod. It was further translated into the focal plane, using an optical microscope with a 1 μm depth of focus. A 2D Dectris Eiger X 4 M (2070 × 2167 pixels, 75 μm width) pixel array detector was placed at 133 mm from the sample allowing to record multiple Bragg peaks simultaneously, in transmission geometry. The peaks appear as soon as Bragg diffraction conditions are met, either during the spatial scanning of the disc across the beam (using a step size of 0.4 μm, for a full scanned area of several 10 × 10 μm^2) or during the rocking curve acquisition performed over an angular range of 3°, with an angular step of 0.1° and an exposure time of 0.1 s/step. For the prism, the step size, the angular range and the angular step were set to 0.5 μm, 7° and 0.2°, respectively.

3. Results

The results reported herein have been obtained on the youngest possible prismatic units of *P. margaritifera* and *P. nobilis* shells. These two species have been chosen for the morphological similarities in their prismatic layers, enabling complementary and comparative studies, and for the favourable access to early mineralizing stages. For *P. margaritifera*, juvenile specimens produced by a hatchery were selected and the regions in the vicinity of the growth edge of the shell were chosen for the analysis. The structure of this specific region is illustrated in Supporting Fig. S1. The shell presents a continuous growth history with the bulk of the shell being composed of well-developed and tightly-packed prisms (typical size of about 20 μm), while the growth edge exhibits isolated, smaller and rather disc-like units, which we refer to as discs. Those are the early-stages of the prismatic units [14,44,57]. Note the ring-like features observed on the external side of the shell, as observed previously [14,16]. While similar regions are difficult to access on the shell of *P. nobilis*, we could easily extract the most-recently produced spines (according to the wording introduced by Marin et al. [58],) covering the outer surface of the shells (Methods). Although not often studied, those thin spines (about 30 μm thick at the outer edge) are composed of a single layer of prismatic calcite units, with their morphological appearance comparable to the one of *P. margaritifera* prisms (Supporting Fig. S2). In the following we present the structural results obtained on *P. margaritifera* and *P. nobilis* prisms, using chemical and crystalline sensitive approaches.

### 3.1. Chemical information derived from coherent Raman microscopy

The chemical structure of the shells has first been investigated with coherent Raman scattering microscopy techniques, able to target specific chemical bond vibrations with a spectral resolution of about 12 cm^{-1} (Supporting Fig. S3), using the coherent superposition of two laser pulses, one at a wavelength of 1032 nm and another tunable one in the 730–960 nm range. The high-sensitivity and high-spatial resolution ($\approx$ 350 nm laterally and $\approx$ 2.5 μm axially) of the coherent Raman process allow us to image a 3D volume within a few tens of minutes, with negligible radiation-induced damage. This is a particular advantage for shells, which are rather non-planar and possibly inclined by a few degrees with respect to the plane perpendicular to the beam.

Fig. 1 presents the growth edge of a juvenile *P. margaritifera* shell, obtained in transmission at the calcite symmetric C-O stretch (ν_1) mode (referenced [55] at a wavenumber of 1085 cm^{-1}). As expected, it shows the presence of well-defined densely-packed prisms, constituting the external mineral layer. Closer to the shell edge, disc-like units are observed, which correspond to the early formation stages of the prisms [14,44,57]. Discs of smaller diameter are located closer to the shell edge. While their apparent thickness is limited by the axial resolution of the microscope (see cross-section in Fig. 1C), one can estimate (from de-convolution principle) the disc thickness to about 0.5 (± 0.3) µm, at the edge, and the thickest prisms to be a few microns thick. The elongated units, visible at the very border of the periostracum, on two different cross sections in Fig. 1A-D, are disc units perpendicular to the plane view [4]. The same approach was used on the thicker prisms of the *P. nobilis* shell (Fig. 1E, F), allowing for the 3D representation of the spatial distribution of the intensity. However, the axial resolution, which is intrinsically much larger than the sub-micrometric lateral resolution, prevents a full analysis of the internal intensity distribution of the prisms. Therefore, our further analysis is based on 2D images, obtained after removing the out-of-the-shell-plane parasitic signal and integrating the intensity along the thickness direction. The high lateral spatial resolution of coherent Raman microscopy allows observing black rings, visible in all discs and some prisms of *P. margaritifera* (Fig. 1D) and in some prisms of *P. nobilis* (Fig. 1E). They indicate a lack of locally organized CaCO$_3$ material. Interestingly, in *P. margaritifera*, the shape of these rings clearly starts to show occasional deviation from an annular form when approaching a disc/disc or a disc/prism interface (further illustrated in Supporting Fig. S4). A light etching of the shell enhances those ring-like concentric structures, which are only visible from the external side of the shell (Supporting Fig. S5). A careful analysis of the coherent Raman integrated intensity map was finally performed. We analysed the average intensity further by a histogram approach as a mean to extract the amount of mineral present (Fig. 1H). We observed that individual mineral units are often characterized by a uni- or bimodal intensity distribution. Moreover, in most cases, the maxima of the intensity distribution seem to follow a linear progression (constant increment between two successive maxima, highlighted by grey lines in Fig. 1H). One notes that some prisms however deviate from this behaviour by a small offset. We stipulate that this specific behaviour of the integrated intensity (*i.e.*, the linear progression of the intensity maxima observed in the individual histograms) is likely resulting from the biomineral structure along the growth axis, likely in relation with a laterally non-continuous distribution of mineral. This is further investigated below.

Using the chemical sensitivity of coherent Raman microscopy, a spectral investigation of the same area was performed in the vicinity of the calcite C-O bond ν_1 vibration (Fig. 2): images at different wavenumbers have been recorded and spectra have been extracted at different positions along a section of a mineral unit, located between the disc-like unit region and the mature prism region. The series of spectra shows a broad line profile with a main peak corresponding to the calcite ν_1 vibration, and a second less intense one, shifted towards smaller wavenumbers (at about 1073 cm^{-1}). This value fits the range of previously reported biogenic amorphous CaCO$_3$ vibrations (a broad (30 cm^{-1}) peak at about 1080 ± 5 cm^{-1}, corresponding to the symmetric C-O stretch in a non-symmetric structure) [38]. The presence of this amorphous component was further confirmed by classical Raman microscopy (see Supporting Fig. S9). Therefore, we can safely assign the off-calcite contribution found by coherent Raman microscopy to an amorphous CaCO$_3$ state and further refer to it for readability, as ACC (for amorphous calcium carbonate), while the spectral component corresponding to the ν_1 vibration of calcite (1085 cm^{-1}) is referred to as CC (for

crystalline calcite). In order to quantify the ACC and CC contributions we developed an analysis routine based on the calculation of the symmetric difference map. This contrast map corresponds to the difference between the intensity maps measured at the two selected wavenumbers, normalized by the sum of the two intensity maps. When CC is taken as the reference, a signal fully dominated by the CC (resp., ACC) contribution would result to a +1 (resp., −1) unit-less value, while the value 0 would indicate equivalent contributions of CC and ACC. This is not valid anymore if the widths of the peaks produce an overlap between the respective signals. In this case, the complete absence of one of the components will result in a smaller maximum contrast value, which would be homogeneous over the sample surface if this characteristic is verified all over the sample. Finally, note that if both CC and ACC are present in all positions within the sample, with only slightly different distributions, the CC and ACC maps are expected to present rather similar behaviors. Our analysis approach was carefully tested on numerical data (Supporting Fig. S6): it allows extracting some contrast information without prior knowledge on the intrinsic width of the two considered peaks. The contrast maps shown in Fig. 2E-G exhibit some inhomogeneities: the mineral units appear mostly crystalline, however with some ACC rich regions present at their edges. In a second analysed shell, presented in Supporting Fig. S7, we observed that the discs closer to the growth edge contain a larger amount of ACC. Some ring-like regions centred on the mineral units and corresponding to an increase of ACC are also observed. For both *P. margaritifera* samples, we note that some of the ACC enrichment seems to be close to the black ring structures. A specific noise analysis was performed in order to address the origin of the observed fluctuations in the contrast map and ensured that their values were significant (Fig. S8A, B). Note that the investigation of a mature (thick) prism (Fig. S7G-I), although it evidences also the presence of ACC-enriched regions (rather in the centre of the prism and in the interprismatic regions), does not allow us to distinguish the ring-like features anymore. To go further in the analysis, the Amide I region [59] at 1650 cm^{-1} was targeted. We referred to it as Pr (standing for proteins, based on the presence of amide groups in their structure). Displayed in Fig. 2D, an inhomogeneous distribution of Pr is observed inside the mineral units, which resembles the previously found distribution of ACC, evidenced by the contrast map in Fig. 2E. This is further highlighted by the direct comparisons performed for some individual mineral units in Fig. 2F and G. To allow for a better quantification of this correlation, the correlation coefficients, between the contrast map and the Pr map, were calculated for a series of mineral units (Supporting Fig. S8C, D). As a strong structural contrast is already present at the border of the individual prisms, producing a systematic bias in the correlation coefficient, the calculation of the correlation coefficient is restricted to regions inside the prism. They are all clearly negative (note that, the correlation coefficients obtained between the contrast map and the CC maps are all clearly positive). A comparable study was performed on the *P. nobilis* shell spine (Fig. 3). As observed for the *P. margaritifera* shell, the CC distribution map shows a decrease of CC intensity in annular regions. The comparison with the ACC and Pr maps shows that the regions with reduced CC-content are generally associated with excess in Pr and ACC (Fig. 3D, E). This was further quantified by calculating the correlation coefficients (Supporting Fig. S8E, F), which present a behaviour similar to the one observed for *P. margaritifera*, confirming this trend. The observation of a Pr signal in the interprismatic regions is consistent with the presence of the organic matter constituting the prism envelope [60,61]. Unfortunately, going further in the analysis of the organic composition is likely out of our reach at this stage, as this would require a highly-sensitive and spatially highly-resolved approach able at producing extended chemical information. A classical Raman spectroscopy characteriza-
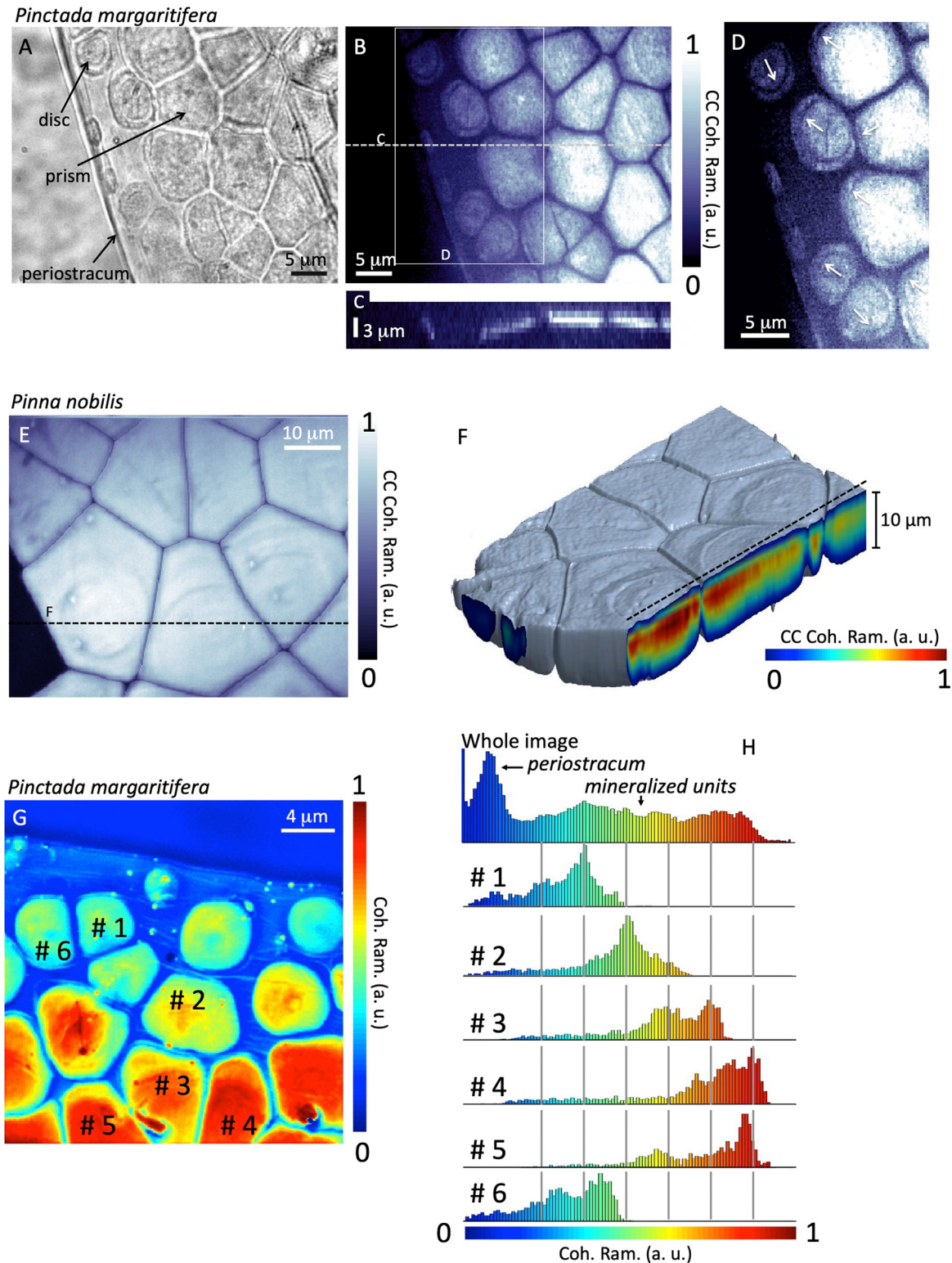
Fig. 1. Coherent Raman microscopy of the growth edge of a *Pinctada margaritifera* shell and the shell spine of *Pinna nobilis*. (**A**) Optical micrographs of a juvenile *P. margaritifera* shell in the vicinity of its growth edge. Well-defined polygonal prisms and disc-like units, the early mineralization stage of prisms, can be identified. The limit of the periostracum supporting membrane is also visible. (**B**) Same shell area, investigated with Coherent anti-Stokes Raman scattering (CARS) at the symmetric stretch C-O (ν_1) vibration mode of calcite (see text). (**C**) Cross section of the 3D acquisition along the line indicated in (**A**). An about-to-flip disc-like unit is visible at the shell edge. Note that the horizontal scale in (**C**) is the same as the one in (**B**). The intensity colour scale for (**B**) and (**C**) is shown in (**B**). (**D**) Zoom-in view with slightly enhanced intensity contrast. Black rings corresponding to calcite-reduced regions are visible in some disc-like and prism units, at the shell border. (**E**) Same approach performed on a *P. nobilis* shell spine. (**F**) 3D volume rendering of the 3D CARS signal. The grey surface corresponds to region with the same intensity level. (**G, H**) Histogram analysis of the coherent Raman intensity signal shown in (**G**), obtained with the stimulated Raman scattering (SRS) modality. The histograms refer to individual prisms identified in (**G**). The grey lines are guides to the eye. The intensity colour scales, common to (**G**) and (**H**), are indicated on the plot. (For interpretation of the references to colour in this figure legend, the reader is referred to the web version of this article.)

Pinctada margaritifera
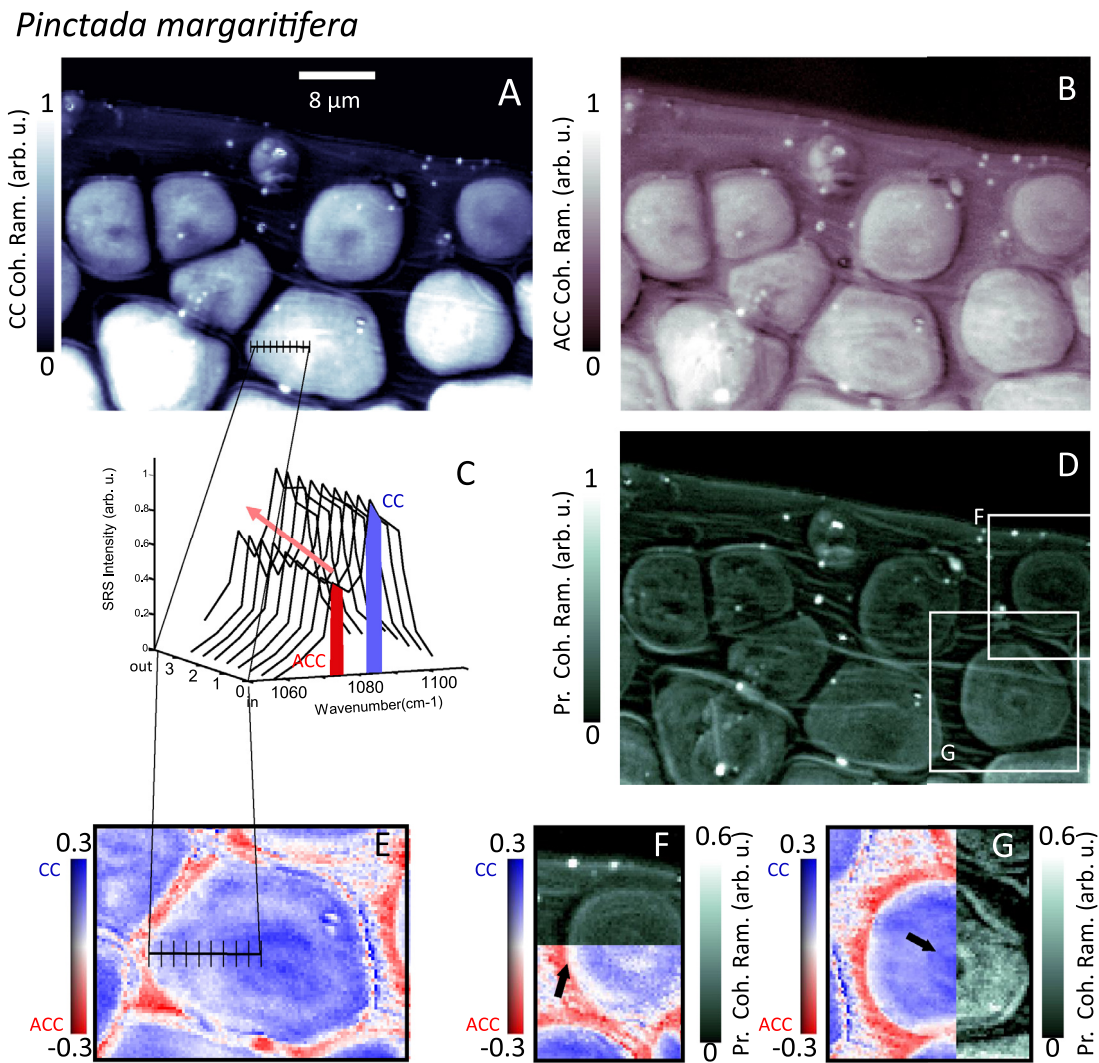
Fig. 2. Coherent Raman microscopy images performed at the calcite ν_1, the amorphous calcium carbonate ν_1 and the Amide I vibration modes on a *Pinctada margaritifera* shell. (**A**) SRS intensity image of a *P. margaritifera* growth edge, obtained at the symmetric stretch C-O (ν_1) vibration (1085 cm^{-1} for crystalline calcite (CC)). (**B**) Same area measured at the amorphous calcium carbonate (ACC) ν_1 vibration (1073 cm^{-1}). (**C**) Full spectra obtained for different positions along a prism radius identified in (**A**). (**D**) Same area as (**A**) and (**B**) measured at the Amide I vibration (1650 cm^{-1}) and referred to as Pr (for proteins). For (**A-C**) the linear intensity scale is indicated on the plots. (**E**) The normalized intensity difference (signal symmetric difference) calculated from images obtained near 1085 and 1073 cm^{-1}, for an individual prism. The hue values encode the amount of crystalline calcite (CC) material *versus* amorphous calcium carbonate (ACC), while the brightness corresponds to the CC intensity signal. (**F, G**) *left* same as (**E**) for other mineralized units and (in green) the corresponding juxtaposed Pr maps. The black arrows in (**F**) and (**G**) point towards regions presenting ACC enrichment. (For interpretation of the references to colour in this figure legend, the reader is referred to the web version of this article.)

tion, performed on a *P. margaritifera* shell, is presented as Supporting Fig. S9. Besides evidencing the usual organics-related bands, it confirms the presence of ACC within the investigated disc.

In summary, coherent Raman microscopy allowed evidencing the presence of the ring-like features in early mineralizing units of *P. margaritifera* and thin prisms *of P. nobilis*. These ring-like features are characterized by a decrease in CC and an increase in ACC and Pr and they start to deviate strongly from their initial annular shape once the mineralizing units get in contact with each other.

3.2. Crystalline information from optical vectorial ptychography

The crystalline structure of these shells was further investigated with optical vectorial ptychography, a recently developed quantitative microscopy approach, conceived for mapping the optical response of optically anisotropic materials [48,62]. Experimental and algorithmic details are given in the Methods. Results presented

here exploit the most advanced methodological development aiming at extracting structural information from these data [49]. Following this approach, we focus on the optical path length (OPL), the retardance (R) and the Eigen-polarization ellipticity (EPE), defined as follows. For a material homogenous in depth, the OPL reduces to ($n_o \cdot t$), where n_o is the ordinary optical refractive index (for pure calcite, $n_o = 1.658$) and t the total thickness. The retardance R is defined by ($|\Delta n_{eff}| \cdot t$), where Δn_{eff} is the effective birefringence, resulting from the angle between the beam direction and the c-axis of the calcite crystal (see Supporting Fig. S10). Note that, for an optically isotropic material (*i.e.*, the amorphous phase, here) $\Delta n_{eff} = 0$ and so is the retardance. The EPE is related to the crystalline disorder along the beam direction. For a crystal perfectly homogeneous in depth, the EPE is zero, while larger values evidence that the direction of the c-axis crystal, as projected in the sample plane, varies significantly along the sample depth [49]. Note that, if R = 0 (isotropic material or beam direction par-
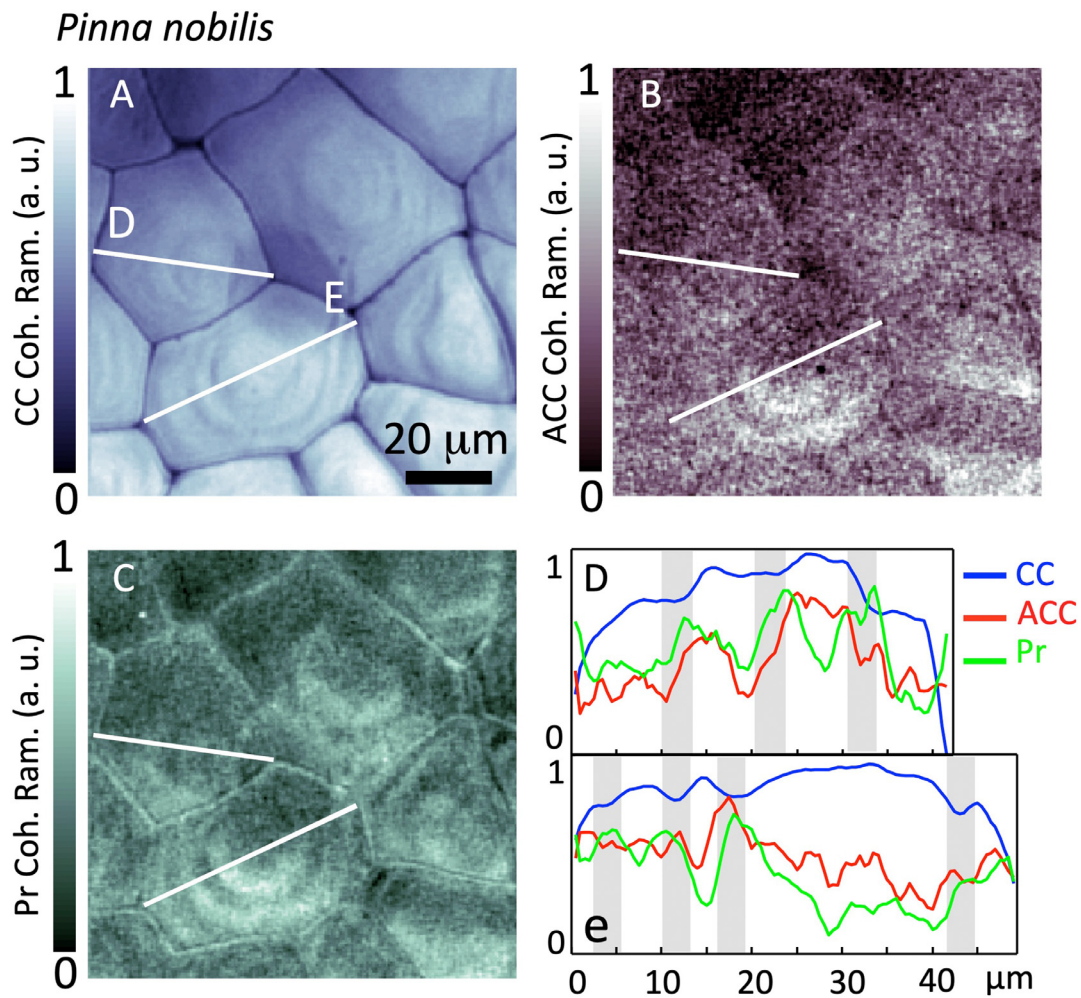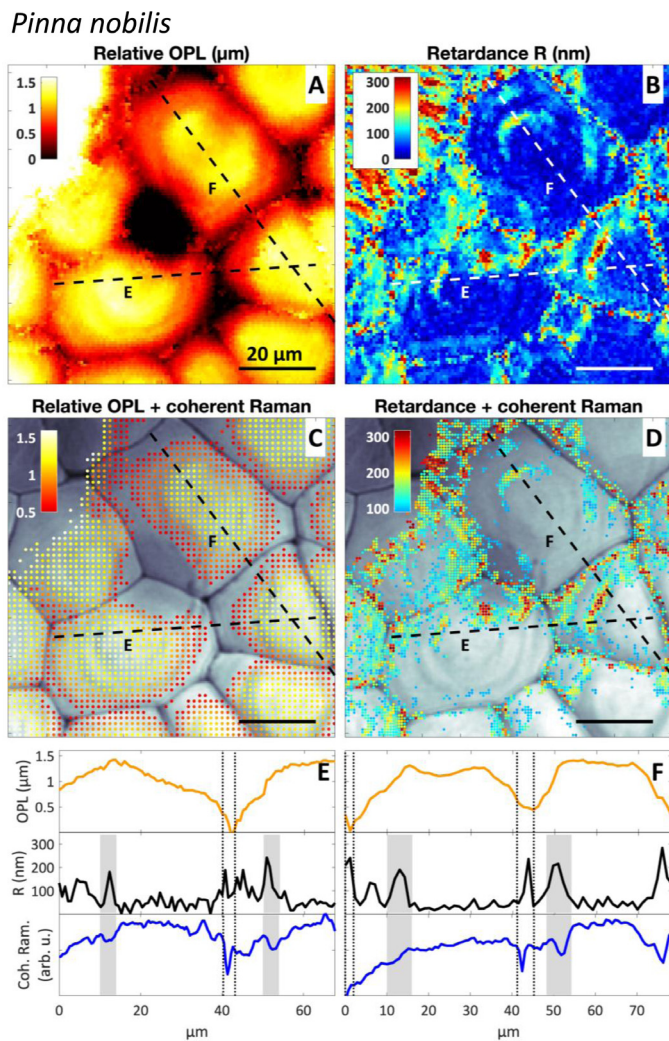
Pinna nobilis

Fig. 3. Coherent Raman microscopy images performed at the CC, ACC and Pr vibration modes on a *Pinna nobilis* shell spine. (**A**)-(**C**) SRS intensity images of a *P. nobilis* spine at the CC, ACC and Pr vibration modes, respectively. (**D, E**) Cross sections of the signals shown in (**A**)-(**C**), along the lines indicated in (**A**). These plots show some correlation between the ACC and Pr signals and their anti-correlation with the CC signal. Linear colour scales (a.u.) and spatial scales are indicated.

allel to the c-axis), the EPE value is meaningless, because of degeneracy [49]. Finally, the transmittance, which is another parameter extracted from this analysis, describes the transmission power of a sample (from opaque to transparent). This quantity provides images similar to wide-field optical images and contains little physical information. It is shown hereafter as a mean to depict the shell morphology. The results obtained on the same *P. nobilis* shell already investigated with coherent Raman (Fig. 2) are shown in Fig. 4 and Supporting Fig. S11, while the investigation of a *P. margaritifera* growing shell edge is presented in Fig. 5. The OPL provides information on the optical properties integrated along the prism thickness, and its mapping can evidence small lateral fluctuations within a prism: the OPL precision is about a few nanometers while, laterally, it presents the sub-micrometric lateral resolution of optical microscopy. For each prism, we observe a dome-like OPL profile (Fig. 4A and Supporting Fig. S11B and C), exhibiting approximately the same amplitude between the centre and the edge of the prisms, irrespective of the distance from the shell border (the height of the dome would be at most about 100–500 nm, assuming the material producing the dome-like OPL profile is pure calcite, which is likely an overestimation of the biogenic calcite index). The retardance is reported in Fig. 4B. As the extraordinary axis, corresponding to the c-axis of the crystal, is mostly aligned with the beam observation direction, the resulting retardance is on average negligible in most of the observed prisms (similar to

the sketch in Supporting Fig. S10A). However, a closer look within the prisms unveils local annular features of larger retardance, suggesting local change in the crystalline orientation properties. These observations can be compared with the above coherent Raman microscopy results, presented in Fig. 2 (Fig. 4C, D), where the retardance map, limited to higher values, has been superimposed onto the CC chemical map of the same region (Fig. 4D). This comparison highlights the strong correlation between the chemical and crystalline features within the prisms. Results obtained on the *P. margaritifera* shell (Fig. 5) show similar behaviour with respect to the dome-like profile. However, the whole retardance map, where most of the prisms present non-zero retardance, is rather different from the *P. nobilis* one. The retardance map of the whole prismatic assembly results from a larger range of orientational distribution with respect to the orientation of prisms in *P. nobilis*, in agreement with literature [50]. For this shell, whose R is mostly non-zero (Fig. 5C), the EPE map is also shown (Fig. 5D). Closer observations of some individual prisms are plotted in Fig. 5E-I, focusing either on R or EPE. For prisms with R ≈ 0, one often observes some faint annular rings within the prisms (Fig. 5E, F). When R ≠ 0, the measurement is less sensitive to small changes of R and we thus rely on the EPE map. The prisms selected in Fig. 5G-I are characterized in general by very small EPE values, contrasting with some annular structures corresponding to a local increase of the EPE. These annular structures, observed in the R and EPE maps,

Pinna nobilis

Fig. 4. *Pinna nobilis* spine as seen by optical vectorial ptychography. (**A**) Optical path length (OPL) and (**B**) retardance (R) maps obtained on the same *Pinna nobilis* shell spine as shown in Fig. 3. (**C, D**) OPL and R maps, restricted to higher values and superimposed onto the coherent Raman map acquired at the CC vibration mode (Fig. 3A), in order to highlight correlations with the CC coherent Raman distribution map. (**E, F**) Profile plots along the dashed lines indicated in (**C**) and (**D**). The grey areas highlight regions within the prisms where an increase of retardance correlates with a decrease of the CC signal, while dotted lines define the inter-prismatic regions, for which the OPL is small and therefore, R becomes noisy. Colour scales are indicated on the figures. In (**A-D**), the scale bars are 20 μm. (For interpretation of the references to colour in this figure legend, the reader is referred to the web version of this article.)

result from local crystalline disorder along the beam direction, *i.e.*, along the prism thickness.

In brief, the crystalline characterization of the prisms from both species evidenced a dome-like OPL profile and the presence of local annular features of larger retardance visible in prisms of small retardance or similar annular features in the EPE map, for prisms of larger retardance. These likely result from crystalline disorder along the mineralizing unit thickness.

3.3. Crystalline information derived from X-ray nanoprobe Bragg diffraction
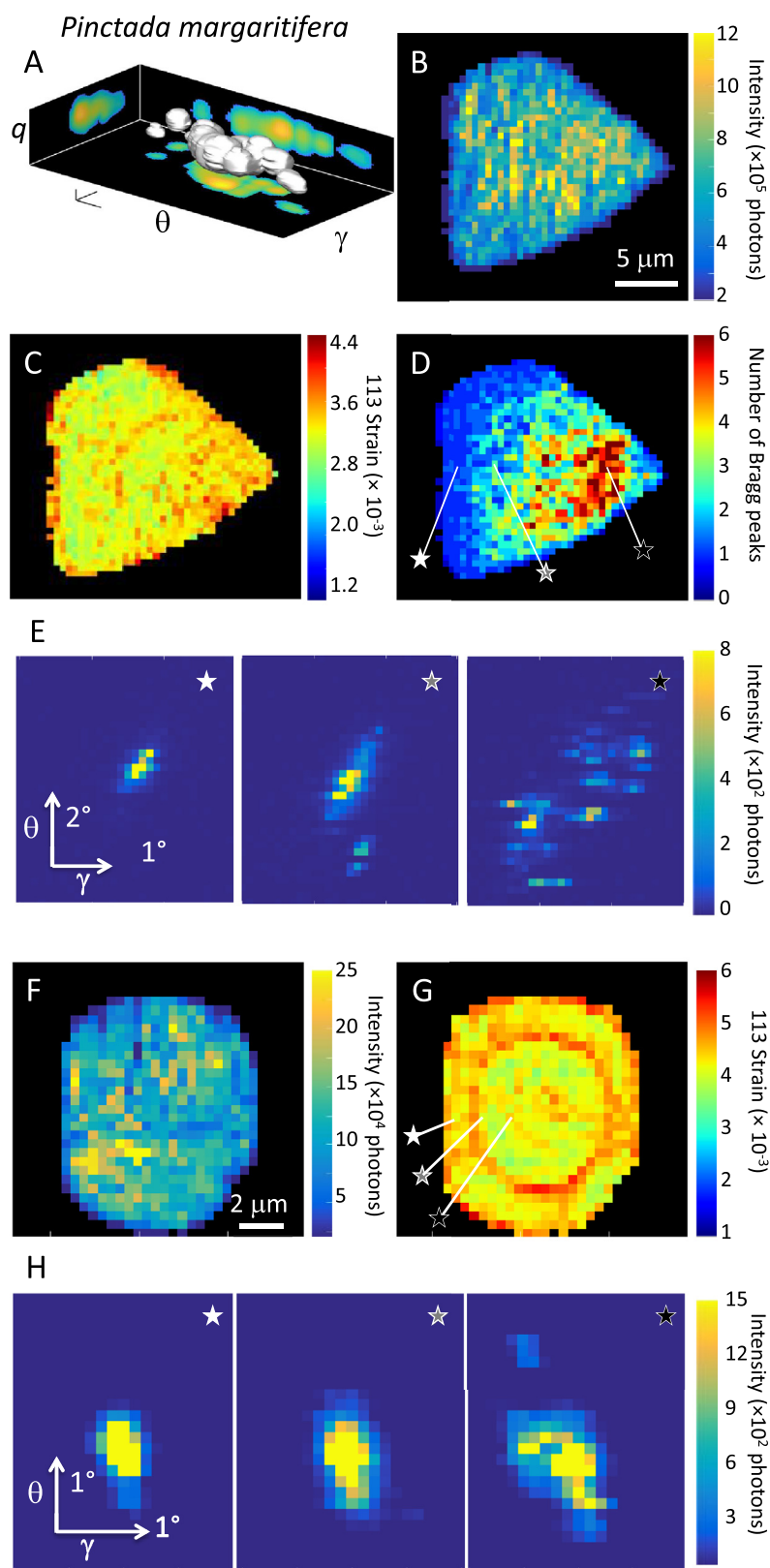
Finally, X-ray nanoprobe Bragg diffraction experiments were carried out on disc and prism units of a *P. margaritifera* shell as a mean to further investigate the crystalline properties in these early mineralized units, without intrusive sample preparation. The pen-

Pinctada margaritifera
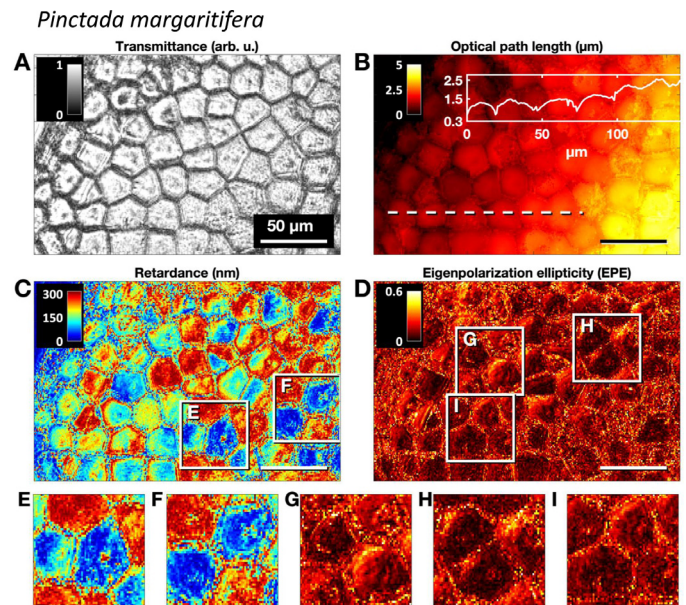
Fig. 5. Optical vectorial ptychography characterization of a Pinctada margaritifera shell growth edge. (**A**) Transmittance map. (**B**) OPL map and cross-section (inset) obtained along the white dashed line shown in (**B**). (**C**) Retardance (R) map evidencing large retardance distribution, likely resulting from the wide distribution of the c-axis orientation[50]. (**D**) Eigen-polarization ellipticity (EPE) map. (**E, F**) Retardance zoom-in views, centred on prism units with low retardance. The colour scale is the same as in (**C**). These prisms are particularly sensitive to structural defects due to their generally low level of retardance. (**G-I**) EPE Zoom-in views centred on prism units with non-zero retardance. The colour scale is the same as in (**D**). In (**E-I**) some faint annular structures are sometimes visible. Note that R and EPE can not be reliably evaluated in regions where OPL is small (as *e.g.*, the inter-prismatic regions). The scale bars are 50 μm. (For interpretation of the references to colour in this figure legend, the reader is referred to the web version of this article.)

etration power of the 14.64 keV X-ray beam enables the investigation of native shells, giving access to the integral crystalline properties along the X-ray beam, *i.e.*, along the thickness. The method is furthermore highly sensitive to crystalline strain (within a few 10^{-4} accuracy) and tilts (a few $0.001°$). The spatial resolution is ultimately limited by the size of the beam (about 80 nm) and the field of view is typically in the 10 - 100 μm range, making it suitable to explore a full mineralized unit. The highly focused nanobeam is scanned across the sample while rocking the sample to explore different orientations of the crystal, over a limited angular range of a few degrees. As each mineralized unit has a different crystalline orientation, its Bragg diffraction peak contribution can be isolated and analysed separately from the ones arising from the neighbouring units. At each scanning position, the 3D intensity distribution is recorded in the vicinity of a Bragg reflection, a typical example of which is shown in Fig. 6A, together with the three associated planar projections (defined by the lattice distortion- (or strain-) related axis q and the two rotation axes θ and γ): it highlights the complexity of the intensity distribution, being composed of several distinct Bragg peak components. For both prism and disc, the integrated Bragg diffraction intensity distributions follow the shape of the units they stem from, indicating a rather homogenous orientation of the probed crystalline planes (Fig. 6B, F). From the 3D intensity distribution, the lattice distortion over the prism and disc areas can be calculated, defined as $\Delta d_{hkl}/d_{hkl}$ with $\Delta d_{hkl} = d_{ref} - d_{hkl}$ and d_{hkl} (resp., d_{ref}) being the lattice parameters in the disc or prism, estimated from the Bragg peak position (resp., the lattice parameter of a chosen crystalline reference). For all analysed hkl reflections, the mean position of the Bragg peaks allows us to calculate an average compressive lattice distortion of about $(3.7 \pm 0.5) \times 10^{-3}$ using the geological calcite

Fig. 6. X-ray nanoprobe Bragg diffraction investigations of a disc and prism from a *Pinctada margaritifera* shell. (**A**) Typical 3D intensity distribution obtained at the 125 Bragg reflection, for a single position of the nanobeam onto the sample. It shows the complexity of the Bragg peak along the strain-related axis q, the rocking curve angle θ and the azimuth angle γ. The projections onto the three planes defined by these axes are also shown. The scale bars along θ and γ represents 0.5°, while the one along q represents 0.41 nm^{-1}. (**B**) Spatial distribution of the integrated diffraction intensity from the 113, 125 and 204 reflections, for the prism. (**C**) Strain extracted from the 113 intensity distribution. (**D**) Number of peaks (or components) observed in the 3D Bragg intensity distribution: the shown numbers are the average values obtained from the 113, 125 and 204 reflections. (**E**) Typical evolution of the Bragg diffraction intensity (125 reflection projected onto the (θ, γ) plane) along an axis parallel to the shell growing direction. The respective beam positions are indicated in (**D**). (**F**) Same as (**B**) for the disc 113 reflection. (**G**) Strain map extracted from the 113 reflection. (**H**) Same as (**E**) for the disc (113 reflection), with respective beam positions indicated in (**G**). In (**C**) and (**G**), the colour scale has been chosen so that the zero value refers to the same geological calcite reference, while the colour range has been set so that the ring-like feature and the average strain level exhibit the same contrast.

crystalline parameters as a reference. It means that the found lattice parameters is smaller than the one of geological calcite. Interestingly, the distortion maps exhibit full or partial ring-like structures (Fig. 6C, G). A full ring is observed for the disc, while a partial annular feature is observed for the prism, located on the prism part, which is closer to the shell growth edge. This feature, which corresponds to a shift of the Bragg peak position with respect to the mean position defined previously, is an additional compressive strain of about 1.8×10^{-3}. For the prism, this feature is not visible in the 125 distortion maps, but still on the 113 and 204, likely indicating that the additional strain develops mostly along the calcite a- and/or b-axis, as a- and b-axis information contributes slightly more strongly to the 113 and 204 Bragg peak positions. Finally, the number of Bragg peak components was extracted from the series of 2D intensity maps projected along the strain-related direction, *i.e.*, onto the plane defined by the two rotation axes (shown for the prism in Fig. 6D). This map presents a specific spatial distribution pattern, with the number of components, within one prism, increasing from the shell growth edge towards the more mature part of the shell, starting with only one Bragg peak at the prism region closer to the growth edge, up to about 6 peaks further away from the growth edge. In comparison, the disc exhibits a smaller number of peak components, estimated as one or two, within the limit of the data quality (Supporting Fig. S12).

In summary, the crystalline characterization of *P. margaritifera* early mineralizing units evidenced again the presence of ring-like features, appearing as a local increase in the strain map. The Bragg peak intensity distribution, which can be monitored over the unit area, is composed of several contributions. While the number of contributions is rather small in the disc, it evolves strongly in the prism, up to several peaks in the part opposite to the growth edge.

3.4. Complementary crystalline information derived electron microscopy

As a complementary approach, transmission electron microscopy (TEM) was used to gain insights on the initial stages of the biomineralization process (Supporting Figs. S13–15). To this aim, a well-developed prism was selected and the area in vicinity to the external side of the prism was investigated with electron beam diffraction, a region identified as the starting point of the prism growth (see Supporting Fig. S1D-F). It reveals the presence of a nodule on the external surface of the prism. Upon close inspection beneath the nodule, a layered, rather irregular, organization of the mineral material took place along the prism depth. Such layers, although difficult to identify, could be about 150 to 300 nm in thickness and the first deposited layers seem to present an arcuate shape following the inner side of the nodule (see Supporting Fig. S13 and S14D). Unfortunately, the characterization of additional nodules could not be produced, likely because the success of this challenging experiment requires that the nodule is still present on the surface prior to the invasive sample preparation, while the centre of the prisms often presents a depletion on their external side (see Supporting Fig. S1). Furthermore, the position of the axial section needs to be matched to the nodule within a few hundreds of nanometers accuracy. Additional investigations performed on the external sub-surface of a prism are shown in Supporting Fig. S15, together with a series of close-up views of the granular structure, along the prism's radial direction up to the prism edge. It exhibits a crystalline-to-amorphous transition towards the prism edge. More details on these results are presented in the caption of Fig S15.

In short, the observation of a prism cross section with electron transmission microscopy, performed in the vicinity of the external side of the prism, shows the presence of a nodule on the top of crystalline layers with possibly arcuate shape. At the prism edge, a
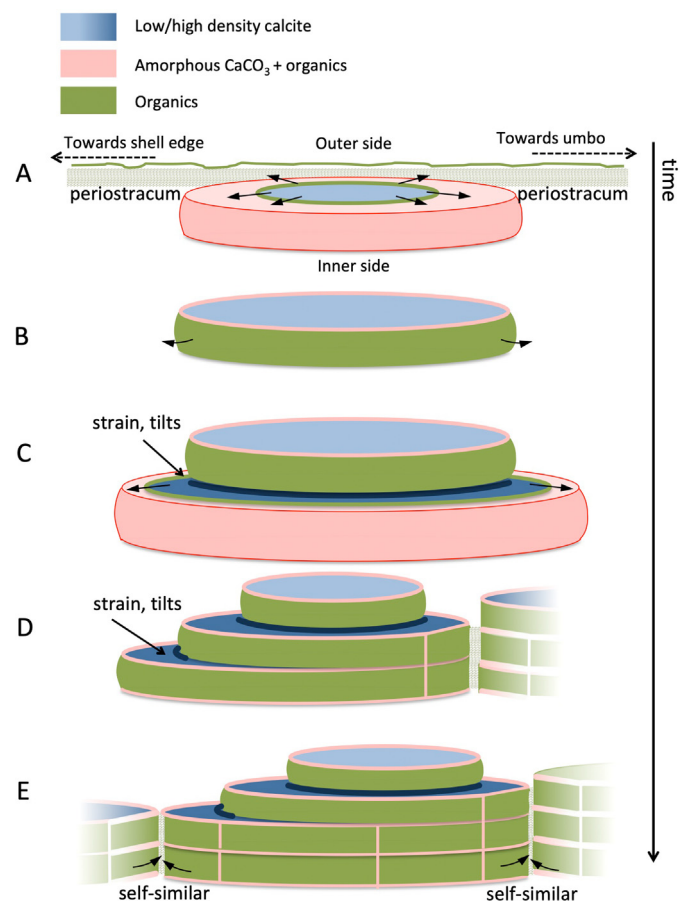
Fig. 7. Proposition of a temporal model of prism formation in early stages. (**A**) Initial disc formation resulting from the transformation of a mixture of amorphous $CaCO_3$ and organics into calcite, following a radial progression and a radial exclusion and thus transport of organics towards the disc edge. (**B**) At the end of the transformation, the disc is mostly crystalline with un-transformed amorphous and organics at the edge and organics expelled further outside. (**C**) A subsequent layer forms underneath the first layer, following the same transformations as described in (**A**), with likely a higher crystalline density and a larger lateral extent, resulting in a dome-like height profile. The crystal quality under the edge of the previously formed disc is modified locally (strain and tilts), in the vicinity of the organic-rich region. (**D**) Subsequent layers forms following the same transformations as described in (**A**) and (**B**). Their lateral extent is limited by the nearest neighbors, in the region opposite to shell growth edge. It results in the formation of flat interfaces and the transformation from the disc to the prism shape. Organics accumulate in the inter-prismatic region. (**E**) The prism grows by self-replication.

gradient of crystallinity is observed, from fully crystalline granules to fully amorphous.

4. Discussion

4.1. Analysis of the observed chemical and crystalline structural features

The chemical and crystalline features identified in early biomineralized units shed light on the process of biomineralization, which we discuss further. To support our analysis and help the reader to follow our reasoning, we summarize our propositions in a 3D biomineralization model, depicted in Fig. 7, inferring the behaviour in the third direction by considering the changes observed between young disc-like units and mature prisms. Starting from the results depicted in Fig. 1 (and Supporting Figs. S4 and S5), we observed that the ring-like features, identified by chemical and crystalline contrast techniques, start to deviate strongly from their initial annular shape once mineralizing units get in contact with each

other. This behaviour likely indicates that the rings progress radially from a centre to the edge of the mineralizing unit (Fig. 7A, B). This notion of radial growth is also supported by the difference in the strain distributions observed in the disc (full ring) and the prism (partial annular feature, located inside the prism). This is likely resulting from the Voronoi growth process [63,64], showing that the prism continues to extend in space if unabutted. The frequent observation of ACC at the prism edges and in early discs (Fig. 2 and Supporting Fig. S7) could further indicate that ACC precursors are involved in the crystallisation process of *P. margaritifera* and *P. nobilis*. The coexistence of Pr and ACC in the CC-reduced regions, further evidenced by the calculation of the correlation coefficients (Supporting Fig. S8) may be interpreted as exclusion of organics as CC crystallises from ACC, from the prism centre to the prism edge, while the presence of ACC at the prism edge might rather be due to the incomplete ACC transformation, at the prism interface. The systematic observation of an overall dome-like OPL profiles in prisms (Figs. 4 and 5 and Supporting Fig. S11) could be attributed to an increase of the disc thickness (Fig. 7C, D) occurring simultaneously with its widening until some part of the disc edge reaches the neighbouring units. Alternatively, an increase of the optical refractive index alone (induced by *e.g.*, the densification of the material), in the central part of the prism, could lead to the same dome-like OPL profile. However, the coherent Raman integrated intensity along the prism thickness, shows, at least for some prisms of *P. margaritifera*, a similar dome like profile, supporting the hypothesis of a prism slightly thicker in its centre than at the edge (and so far not visible with scanning electron microscopy). Along the shell surface, when the mineral units abut one another, their shape is no longer circular. The built interface becomes flat, following a Voronoi-cell construction [63,64] (Fig. 7D, E). The additional depressions observed near the centre of many prisms (with coherent Raman and optical vectorial ptychography microscopy approaches, see *e.g.*, Fig. 4A, E, F or Fig. 5B), coincide well with the centre of a Voronoi-cell ordering pattern and might be attributed to the onset of the disc nucleation process. The nodule observed in Supporting Fig. S13, exhibits low Ca and O contents (below the detection level), which would agree with the presence of organic matter. Although the role of the amorphous nodule is difficult to demonstrate, we would like to suggest that this could be the organic calcification centre, as already proposed by others [12,65], owing to the likely arcuate shape of the crystalline layers underneath the nodule. However, this single observation is not a decisive proof. Finally, optical (Figs. 4 and 5) and X-ray (Fig. 6) microscopy data indicate a modification of the crystalline properties in the vicinity of the ring-like structure, corresponding to both compressive strain and lattice tilts. The observation of the ring-like strain and orientational disorder structures indicates that the crystallisation process is likely modified under or close to the organic-rich regions (Fig. 7C-E). The existence of several Bragg peak components in some regions of the prism indicates that the crystallinity is neither perfectly homogeneous nor continuous along the thickness direction. It rather corresponds to a stacking of crystals with slightly different orientations. However, this behaviour changes strongly along the prism surface. In particular, the region closer to the shell edge is perfectly homogeneous (one Bragg component). In the same way, the disc, which is in total thinner, exhibits a smaller number of Bragg components. These two observations point towards a layer-by-layer growth model, in which each layer, may be arcuate around the nodule for the first crystallisation cycles, would be associated to a slightly different crystalline orientation within the range of about 2–3°. The finite extent of the very first layers and their limited extent when the crystalline unit is in contact with the neighbour units would explain the increase of Bragg components observed in some part of the prism (Supporting Fig. S12F, G), an observation that is also consistent with the

optical dome-like profile. Finally, the histogram analysis performed on the coherent Raman intensity signal, shows that the prism intensity distributions usually exhibit one or two main peaks. The increment between these peaks appears to be relatively constant and follows a linear increase towards mature prisms. Unless it corresponds to an unlikely step-wise progression of the crystal density, this behaviour also supports the layer-by-layer growth model [51,53,66]. A rough estimation of the prism thickness (*e.g.*, about 3–4 μm for prism #4 in Fig. 1G) compared to the position of its intensity distribution maximum (6 intervals, in Fig. 1F) allows us to estimate the individual growth layer to be in the range of 500–600 nm.

4.2. Prism biomineralization temporal model

The possibility to observe several mineralizing units in their early growth stage and to image the distribution of disordered and ordered $CaCO_3$ within each mineralizing units, allows us to propose a temporal sequence, at least within the limits of these indirect observations. Our experimental observations point towards the existence of an amorphous calcium carbonate precursor that would further transform into crystalline $CaCO_3$, after the organics is expelled from the currently growing layer, as already suggested by others [67]. Similar conclusions were inferred from various observations of ACC in a series of biomineral structures [38]. We note that the formation of a transient ACC phase from an initial liquid amorphous hydrated $CaCO_3$ as reported earlier [68], is consistent with our observations: the radial progression of the observed ring and the expulsion of the organics across the mineralizing unit necessitate a substantial degree of intrinsic viscosity in the surrounding material, as it should be provided by a hydrated $CaCO_3$ phase, which was already observed in calcite [32,69] and aragonite [33,37] biominerals or by a dense liquid precursor [70].

The presence of the bent organic feature, coinciding with an increasing amount of amorphous $CaCO_3$ phase and the reduction of crystalline $CaCO_3$, indicates that organic molecules are likely associated to the amorphous-to-crystalline transition, as proposed earlier [71]. The exact role of these organics, whether they stabilize the ACC prior to its transformation into CC, or are released during the transformation, is however difficult to infer. We further propose that the radial motion of the organic ring-like feature and the accumulation of the organic material at the edge of crystallizing unit produce – at least in part - the widely observed [60,61] organic inter-prismatic walls. An additional source of organic molecules arising directly from the mantle cells could complete the inter-prismatic structure by attaching to the prism envelope as it presents itself at the prism surface, in agreement with the observations from others [72,73]. Theoretical works have addressed the question of the prism columnar growth [61,63]. The process we suggest would imply that the columnar shape of the prism assembly results from a mechanism in which the growth of each prism is obtained by replicating the same organic/crystalline morphology, all along the mineralizing cycles. Assuming that the crystallisation mode remains the same along the prism growth (*i.e.*, it relies on an amorphous-to-crystalline transformation progressing radially from a nucleation centre), this necessarily requires the preservation of the ring centre from one mineralizing layer to another. The presence of an organic nodule, which we tend to interpret as the initial nucleation centre (as previously reported [14,74]), may coincide with the ring centre, at least for the initial mineralizing cycle. However, for the subsequent prism growth, the mechanism driving the self-replication of the prism shape is more intriguing. The identification of the organic molecules is out of the scope of the present article. Although challenging to apply to the early disc-like mineralized units, additional information could possibly be gained with spatially-resolved nanoSIMS [75]. Our work

does not investigate further the role of the organic molecules, but the hypothesis we present here opens up several questions, which may guide future experiments. It seems quite unlikely that this persistent registration is induced by the distribution of the mantle cells (this would require the cells to remain at exactly the same position within a positional accuracy in the order of the prism wall sharpness, *i.e.*, likely less than a micrometre, while the whole mantle is growing to accommodate the increasing extent of the shell). One possible scenario would be that the centre of the prism, beyond the initial disc in contact with the organic nodule, corresponds to some variations in chemical composition of the mineralizing part, which would be replicated along the prism axis, preserving the columnar shape. In particular, this nucleation centre could be caused by the presence of organic molecules able to destabilize the amorphous state and trigger the crystallisation. They could be produced by the mantle and self-assembled in spatial registration with an organic nodule. The location of the crystallisation nucleation at the centre of the disc would be further consistent with the ring-like feature and a nucleation event occurring far from the disc edge, as required to produce the simultaneous thickening and broadening of the disc. Alternatively, we may propose that the organics molecules trapped at the inter-prism walls may disfavour the crystal nucleation in their vicinity, thereby favouring its nucleation far away from them, *i.e.*, at the prism centre, in the on-going growth layer. They could also play a role in the self-replication of the prism along its growth axis by attracting the organic molecules expelled from the successive crystallisation events and/or by the mantle, altering the local chemistry (*e.g.*, by producing a pH gradient) and stopping the amorphous-to-crystal transformation. In both cases (centre-driven or organic-wall inhibited crystallisation), the position of the organic wall depends on the mobility of the organics within the crystallizing media.

Finally, the observation of strain and orientation ring-like features is likely related to the presence of the organic-rich regions (the distortion being more visible on the a- and b-axis, substitution of Ca by Mg impurities is likely ruled out [76]). This suggests that the crystallisation process, and in particular the strain and orientation of the produced crystal, could be locally modified by the organics [77]. While the overall homogeneous compressive strain, observed in the whole unit, is likely due to residual organics in the biogenic calcite, as previously reported [77], the spatially well-defined ring-like strain and orientation pattern would rather hint towards a strong organic interaction at the organic/inorganic interfaces. The organic-mediated strain might provide the means to modify the optical and mechanical properties of calcite, in a spatially fine-grained manner [9]. The behaviour of the Bragg component distribution, which strikingly increases along the shell growth axis, points towards the layer-by-layer biomineralization model [53], further supported by the histogram intensity distribution analysis of the coherent Raman signal.

5. Conclusion

We have presented chemical and crystalline features on the structure of the prismatic units of two bivalve shells *Pinctada margaritifera* and *Pinna nobilis*, by using highly sensitive quantitative optical microscopy methods and high-resolution X-ray Bragg diffraction microscopy approach, all able to provide structural information with negligible radiation-induced impacts. Our multimodal strategy, based on the detailed investigations of early-mineralized units, allows us to provide insights into this calcite biomineralization. We believe that these findings present a significant step forward in the understanding of the biomineralization process, as it provides a clear spatial link between the organics, amorphous and crystalline compounds, and likely their respective evolution over time.

Supporting Information Available: The following supporting information is available:

Micrographs of *Pinctada margaritifera* and *Pinna nobilis* samples, Schematic of Coherent Raman microscopy, Coherent Raman images, Correlation coefficient analysis of coherent Raman data, classical Raman microscopy on a *Pinctada margaritifera* shell, Principles of birefringence measurements, Optical vectorial ptychography of a *Pinna nobilis* shell, X-ray nanoprobe diffraction data, Transmission electron microscopy of a *Pinctada margaritifera* prism and axial sections.

Declaration of Competing Interest

The authors declare that they have no known competing financial interests or personal relationships that could have appeared to influence the work reported in this paper.

Acknowledgements

Supplementary materials

Supplementary material associated with this article can be found, in the online version, at doi:10.1016/j.actbio.2022.01.024.

References

[1] S. Weiner, I. Sagi, L. Addadi, Choosing the Crystallization Path Less Traveled, Science 309 (2005) 1027–1028, doi:10.1126/science.1114920.

[2] I. Zlotnikov, V. Schoeppler, Thermodynamic Aspects of Molluscan Shell Ultra-structural Morphogenesis, Adv. Funct. Mater. 27 (2017) 1700506, doi:10.1002/adfm.201700506.

[3] O.M. Boggild, The shell structure of molluscs, D. Kgl. Danske. Vidensk. Selsk. Skr. Natruvidensk. Og Mathem. 2 (1930) 231–236.

[4] J.-P. Cuif, Y. Dauphin, J.E. Sorauf, Biominerals and Fossils Through Time, 1 Edition, Cambridge University Press, Cambridge ; New York, 2011.

[5] Y. Dauphin, The nanostructural unity of Mollusc shells, Mineralog Mag. 72 (2008) 243–246, doi:10.1180/minmag.2008.072.1.243.

[6] S.E. Wolf, C.F. Böhm, J. Harris, B. Demmert, D.E. Jacob, M. Mondeshki, E. Ruiz-Agudo, C. Rodríguez-Navarro, Nonclassical crystallization *in vivo* et *in vitro* (I): process-structure-property relationships of nanogranular biominerals, J. Struct. Biol. 196 (2016) 244–259, doi:10.1016/j.jsb.2016.07.016.

[7] P.U.P.A. Gilbert, S.M. Porter, C.-Y. Sun, S. Xiao, B.M. Gibson, N. Shenkar, A.H. Knoll, Biomineralization by particle attachment in early animals, Proc. Natl Acad. Sci. 116 (2019) 17659–17665, doi:10.1073/pnas.1902273116.

[8] F. Nudelman, N.A.J.M. Sommerdijk, Biomineralization as an Inspiration for Materials Chemistry, Angew. Chem. Int. Ed. 51 (2012) 6582–6596, doi:10.1002/anie.201106715.

[9] I. Polishchuk, A.A. Bracha, L. Bloch, D. Levy, S. Kozachkevich, Y. Etinger-Geller, Y. Kauffmann, M. Burghammer, C. Giacobbe, J. Villanova, G. Hendler, C.-Y. Sun, A.J. Giuffre, M.A. Marcus, L. Kundanati, P. Zaslansky, N.M. Pugno, P.U.P.A. Gilbert, A. Katsman, B. Pokroy, Coherently aligned nanoparticles within a biogenic single crystal: a biological prestressing strategy, Science 358 (2017) 1294–1298, doi:10.1126/science.aaj2156.

[10] A.G. Checa, J.T. Bonarski, M.G. Willinger, M. Faryna, K. Berent, B. Kania, A. González-Segura, C.M. Pina, J. Pospiech, A. Morawiec, Crystallographic orientation inhomogeneity and crystal splitting in biogenic calcite, J. Roy. Soc. Interface. 10 (2013) 20130425, doi:10.1098/rsif.2013.0425.

[11] Y. Dauphin, A. Brunelle, K. Medjoubi, A. Somogyi, J.-P. Cuif, The Prismatic Layer of Pinna: a Showcase of Methodological Problems and Preconceived Hypotheses, Minerals. 8 (2018) 365, doi:10.3390/min8090365.

[12] J.-P. Cuif, Y. Dauphin, G. Luquet, K. Medjoubi, A. Somogyi, A. Perez-Huerta, Revisiting the Organic Template Model through the Microstructural Study of Shell Development in Pinctada margaritifera, the Polynesian Pearl Oyster, Minerals. 8 (2018) 370, doi:10.3390/min8090370.

[13] J.D. Taylor, W.J. Kennedy, The shell structure and mineralogy of the Bivalvia : introduction, nuculacea-trigonacea, Bull. British Museum (Natural History) 3 (1969) 1–125.

[14] J.-P. Cuif, M. Burghammer, V. Chamard, Y. Dauphin, P. Godard, G.L. Moullac, G. Nehrke, A. Perez-Huerta, Evidence of a Biological Control over Origin, Growth and End of the Calcite Prisms in the Shells of Pinctada margaritifera (Pelecypod, Pterioidea), Minerals. 4 (2014) 815–834, doi:10.3390/min4040815.

[15] H.A. Lowenstam, S. Weiner, On Biomineralization, Oxford University Press, 1989.

[16] S.E. Wolf, I. Lieberwirth, F. Natalio, J.-F. Bardeau, N. Delorme, F. Emmerling, R. Barrea, M. Kappl, F. Marin, Merging models of biomineralisation with concepts of nonclassical crystallisation: is a liquid amorphous precursor involved in the formation of the prismatic layer of the Mediterranean Fan Mussel Pinna nobilis? Faraday Discuss. 159 (2013) 433–448, doi:10.1039/C2FD20045G.

[17] C. Grégoire, Structure of Molluscan Shell, in: M. Florkin, B.T. Scheer (Eds.), Mollusca, Academic press, New York; London, 1972: pp. 45–145.

[18] S. Weiner, Aspartic acid-rich proteins: major components of the soluble organic matrix of mollusk shells, Calcif. Tissue Int. 29 (1979) 163–167.

[19] F. Marin, G. Luquet, Molluscan shell proteins, C.R. Palevol 3 (2004) 469–492, doi:10.1016/j.crpv.2004.07.009.

[20] B. Marie, C. Joubert, A. Tayalé, I. Zanella-Cléon, C. Belliard, D. Piquemal, N. Cochennec-Laureau, F. Marin, Y. Gueguen, C. Montagnani, Different secretory repertoires control the biomineralization processes of prism and nacre deposition of the pearl oyster shell, Proc. Natl Acad. Sci. 109 (2012) 20986–20991, doi:10.1073/pnas.1210552109.

[21] M. Suzuki, K. Saruwatari, T. Kogure, Y. Yamamoto, T. Nishimura, T. Kato, H. Nagasawa, An acidic matrix protein, Pif, is a key macromolecule for nacre formation, Science 325 (2009) 1388–1390, doi:10.1126/science.1173793.

[22] G. Falini, S. Albeck, S. Weiner, L. Addadi, Control of Aragonite or Calcite Polymorphism by Mollusk Shell Macromolecules, Science 271 (1996) 67–69, doi:10.1126/science.271.5245.67.

[23] A.M. Belcher, X.H. Wu, R.J. Christensen, P.K. Hansma, G.D. Stucky, D.E. Morse, Control of crystal phase switching and orientation by soluble mollusc-shell proteins, Nature 381 (1996) 56–58, doi:10.1038/381056a0.

[24] R.A. Metzler, J.S. Evans, C.E. Killian, D. Zhou, T.H. Churchill, N.P. Appathurai, S.N. Coppersmith, P.U.P.A. Gilbert, Nacre Protein Fragment Templates Lamellar Aragonite Growth, J. Am. Chem. Soc. 132 (2010) 6329–6334, doi:10.1021/ja909735y.

[25] J. Seto, Y. Zhang, P. Hamilton, F. Wilt, The localization of occluded matrix proteins in calcareous spicules of sea urchin larvae, J. Struct. Biol. 148 (2004) 123–130, doi:10.1016/j.jsb.2004.04.001.

[26] F. Nudelman, H.H. Chen, H.A. Goldberg, S. Weiner, L. Addadi, Spiers Memorial Lecture, Faraday Discuss 136 (2007) 9–25, doi:10.1039/B704418F.

[27] L. Addadi, D. Joester, F. Nudelman, S. Weiner, Mollusk shell formation: a source of new concepts for understanding biomineralization processes, Chemistry (Easton) 12 (2006) 980–987, doi:10.1002/chem.200500980.

[28] M. Suzuki, T. Okumura, H. Nagasawa, T. Kogure, Localization of intracrystalline organic macromolecules in mollusk shells, J. Cryst. Growth 337 (2011) 24–29, doi:10.1016/j.jcrysgro.2011.10.013.

[29] J.J. De Yoreo, P.U.P.A. Gilbert, N.A.J.M. Sommerdijk, R. Lee Penn, S. Withelam, D. Joester, H. Zhang, J.D. Rimer, A. Navrotsky, J.F. Banfield, A.F. Wallace, F. Marc Michel, F. Meldrum, H. Coelfen, P.M. Dove, Crystallization by particle attachment in synthetic, biogenic, and geologic environments, Science 349 (2015) aaa6760.

[30] E. Beniash, J. Aizenberg, L. Addadi, S. Weiner, Amorphous calcium carbonate transforms into calcite during sea urchin larval spicule growth, Proc. R. Soc. Lond. B: Biol. Sci. 264 (1997) 461–465, doi:10.1098/rspb.1997.0066.

[31] Y. Politi, T. Arad, E. Klein, S. Weiner, L. Addadi, Sea urchin spine calcite forms via a transient amorphous calcium carbonate phase, Science 306 (2004) 1161–1164, doi:10.1126/science.1102289.

[32] Y.U.T. Gong, C.E. Killian, I.C. Olson, N.P. Appathurai, A.L. Amasino, M.C. Martin, L.J. Holt, F.H. Wilt, P.U.P.A. Gilbert, Phase transitions in biogenic amorphous calcium carbonate, Proc. Natl Acad. Sci. 109 (2012) 6088–6093, doi:10.1073/pnas.1118085109.

[33] T. Mass, A.J. Giuffre, C.-Y. Sun, C.A. Stifler, M.J. Frazier, M. Neder, N. Tamura, C.V. Stan, M.A. Marcus, P.U.P.A. Gilbert, Amorphous calcium carbonate particles form coral skeletons, Proc. Natl Acad. Sci. 114 (2017) E7670–E7678, doi:10.1073/pnas.1707890114.

[34] C.-Y. Sun, C.A. Stifler, R.V. Chopdekar, C.A. Schmidt, G. Parida, V. Schoeppler, B.I. Fordyce, J.H. Brau, T. Mass, S. Tambutté, From particle attachment to space–filling coral skeletons, Proc. Natl. Acad. Sci. 117 (2020) 12.

[35] I.M. Weiss, N. Tuross, L. Addadi, S. Weiner, Mollusc larval shell formation: amorphous calcium carbonate is a precursor phase for aragonite, J. Exp. Zool. 293 (2002) 478–491, doi:10.1002/jez.90004.

[36] N. Nassif, N. Pinna, N. Gehrke, M. Antonietti, C. Jäger, H. Cölfen, Amorphous layer around aragonite platelets in nacre, Proc. Natl Acad. Sci. 102 (2005) 12653–12655, doi:10.1073/pnas.0502577102.

[37] R.T. DeVol, C.-Y. Sun, M.A. Marcus, S.N. Coppersmith, S.C.B. Myneni, P.U.P.A. Gilbert, Nanoscale Transforming Mineral Phases in Fresh Nacre, J. Am. Chem. Soc. 137 (2015) 13325–13333, doi:10.1021/jacs.5b07931.

[38] L. Addadi, S. Raz, S. Weiner, Taking Advantage of Disorder: amorphous Calcium Carbonate and Its Roles in Biomineralization, Adv. Mater. 15 (2003) 959–970, doi:10.1002/adma.200300381.

[39] F. Nudelman, E. Sonmezler, P.H.H. Bomans, G. de With, N.A.J.M. Sommerdijk, Stabilization of amorphous calcium carbonate by controlling its particle size, Nanoscale 2 (2010) 2436–2439, doi:10.1039/C0NR00432D.

[40] J. Cavanaugh, M.L. Whittaker, D. Joester, Crystallization kinetics of amorphous calcium carbonate in confinement, Chem. Sci. 10 (2019) 5039–5043, doi:10.1039/C8SC05634J.

[41] S. Raz, P.C. Hamilton, F.H. Wilt, S. Weiner, L. Addadi, The Transient Phase of Amorphous Calcium Carbonate in Sea Urchin Larval Spicules: the Involvement of Proteins and Magnesium Ions in Its Formation and Stabilization, Adv. Funct. Mater. 13 (2003) 480–486, doi:10.1002/adfm.200304285.

[42] L. Xiang, W. Kong, J. Su, J. Liang, G. Zhang, L. Xie, R. Zhang, Amorphous Calcium Carbonate Precipitation by Cellular Biomineralization in Mantle Cell Cultures of Pinctada fucata, PLoS One 9 (2014) e113150, doi:10.1371/journal.pone.0113150.

[43] J. Seto, Y. Ma, S.A. Davis, F. Meldrum, A. Gourrier, Y.-Y. Kim, U. Schilde, M. Sztucki, M. Burghammer, S. Maltsev, C. Jäger, H. Cölfen, Structure-property relationships of a biological mesocrystal in the adult sea urchin spine, Proc. Natl Acad. Sci. 109 (2012) 3699–3704, doi:10.1073/pnas.1109243109.

[44] A.G. Checa, C. Salas, E.M. Harper, J. de, D. Bueno-Pérez, Early Stage Biomineralization in the Periostracum of the 'Living Fossil' Bivalve Neotrigonia, Plos One. 9 (2014) e90033, doi:10.1371/journal.pone.0090033.

[45] L.J. de Nooijer, T. Toyofuku, H. Kitazato, Foraminifera promote calcification by elevating their intracellular pH, Proc. Natl. Acad. Sci. U. S. A. 106 (2009) 15374–15378, doi:10.1073/pnas.0904306106.

[46] R. Hovden, S.E. Wolf, M.E. Holtz, F. Marin, D.A. Muller, L.A. Estroff, Nanoscale assembly processes revealed in the nacroprismatic transition zone of Pinna nobilis mollusc shells, Nat. Commun. 6 (2015) 10097, doi:10.1038/ncomms10097.

[47] Cheng, J.-X., Xie, X.S., Coherent Raman Scattering Microscopy, 1st Edition, CRC Press, 2018.

[48] P. Ferrand, A. Baroni, M. Allain, V. Chamard, Quantitative imaging of anisotropic material properties with vectorial ptychography, Opt. Lett., OL. 43 (2018) 763–766, doi:10.1364/OL.43.000763.

[49] A. Baroni, V. Chamard, P. Ferrand, Extending Quantitative Phase Imaging to Polarization-Sensitive Materials, Phys. Rev. Appl. 13 (2020) 054028, doi:10.1103/PhysRevApplied.13.054028.

[50] Y. Dauphin, E. Zolotoyabko, A. Berner, E. Lakin, C. Rollion-Bard, J.P. Cuif, P. Fratzl, Breaking the long-standing morphological paradigm: individual prisms in the pearl oyster shell grow perpendicular to the c-axis of calcite, J. Struct. Biol. 205 (2019) 121–132, doi:10.1016/j.jsb.2019.01.004.

[51] J.-P. Cuif, Y. Dauphin, G. Nehrke, J. Nouet, A. Perez-Huerta, Layered Growth and Crystallization in Calcareous Biominerals: impact of Structural and Chemical Evidence on Two Major Concepts in Invertebrate Biomineralization Studies, Minerals. 2 (2012) 11–39, doi:10.3390/min2010011.

[52] Y. Dauphin, J. Cuif, J. Doucet, M. Salomé, J. Susini, C. Williams, In situ mapping of growth lines in the calcitic prismatic layers of mollusc shells using X-ray absorption near-edge structure (XANES) spectroscopy at the sulphur K-edge, Mar. Biol. 142 (2003) 299–304, doi:10.1007/s00227-002-0950-2.

[53] J.P. Cuif, Y. Dauphin, The Environment Recording Unit in coral skeletons – a synthesis of structural and chemical evidences for a biochemically driven, stepping-growth process in fibres, Biogeosciences 2 (2005) 61–73, doi:10.5194/bg-2-61-2005.

[54] S. Brustlein, P. Ferrand, N. Walther, S. Brasselet, C. Billaudeau, D. Marguet, H. Rigneault, Optical parametric oscillator-based light source for coherent Raman scattering microscopy: practical overview, J. Biomed. Opt. 16 (2011) 021106, doi:10.1117/1.3533311.

[55] G. Nehrke, J. Nouet, Confocal Raman microscope mapping as a tool to describe different mineral and organic phases at high spatial resolution within marine biogenic carbonates: case study on Nerita undata (Gastropoda, Neritopsina), Biogeosciences 8 (2011) 3761–3769, doi:10.5194/bg-8-3761-2011.

[56] A. Baroni, M. Allain, P. Li, V. Chamard, P. Ferrand, Joint estimation of object and probes in vectorial ptychography, Opt. Express, OE. 27 (2019) 8143–8152, doi:10.1364/OE.27.008143.

[57] Paula M. Mikkelsen, Iilya Tëmkin, Rüdiger Bieler, Williams G. Lyons, Pinctada longisquamosa (Gunker, 1852) (Bivalvia Pteriidae), an unrecognized pearl oyster in the western Atlantic, Malacologia 46 (2004) 473–501.

[58] Marin, F., Narayanappa, P., Motreuil, S., Acidic Shell Proteins of the Mediterranean Fan Mussel Pinna nobilis, in: Molecular Biomineralization: Aquatic Organisms Forming Extraordinary Materials, J. Baumgartner, D. Faivre, and W. E. G. Mueller, Springer-Verlag, Berlin Heidelberg, 2011: pp. 353–389.

[59] Gremlich, H.-U., Yan B., Infrared and Raman Spectroscopy of Biological Materials, M. Dekker, New York (USA), 2001.

[60] J.-P. Cuif, A. Bendounan, Y. Dauphin, J. Nouet, F. Sirotti, Synchrotron-based photoelectron spectroscopy provides evidence for a molecular bond between calcium and mineralizing organic phases in invertebrate calcareous skeletons, Anal. Bioanal. Chem. 405 (2013) 8739–8748, doi:10.1007/s00216-013-7312-4.

[61] A.G. Checa, E. Macías-Sánchez, E.M. Harper, J.H.E. Cartwright, Organic membranes determine the pattern of the columnar prismatic layer of mollusc shells, Proc. R. Soc. B 283 (2016) 20160032, doi:10.1098/rspb.2016.0032.

[62] P. Ferrand, M. Allain, V. Chamard, Ptychography in anisotropic media, Opt. Lett. 40 (2015) 5144, doi:10.1364/OL.40.005144.

[63] B. Bayerlein, P. Zaslansky, Y. Dauphin, A. Rack, P. Fratzl, I. Zlotnikov, Self-similar mesostructure evolution of the growing mollusc shell reminiscent of thermodynamically driven grain growth, Nat. Mater. 13 (2014) 1102–1107, doi:10.1038/nmat4110.

[64] T. Ubukata, Geometric pattern and growth rate of prismatic shell structures in Bivalvia, Forma 16 (2001) 141–154.

[65] Wada, K., Initiation of mineralization of bivalve molluscs, in: Omori, M., Watabe, N. (Eds.), The Mechanisms of Biomineralization in Animals and Plants, Tokai University Press, Tokyo, 1980: pp. 79–92.

[66] A. Baronnet, J.P. Cuif, Y. Dauphin, B. Farre, J. Nouet, Crystallization of biogenic Ca-carbonate within organo-mineral micro-domains. Structure of the calcite prisms of the Pelecypod Pinctada margaritifera (Mollusca) at the submicron to nanometre ranges, Mineralog. Mag. 72 (2008) 617–626, doi:10.1180/minmag.2008.072.2.617.

[67] J.P. Cuif, Y. Dauphin, B. Farre, G. Nehrke, J. Nouet, M. Salomé, Distribution of sulphated polysaccharides within calcareous biominerals indicates a widely shared layered growth-mode for the Invertebrate skeletons and suggest a two-step crystallization process for the mineral growth units, Mineral. Mag. 72 (2008) 233–237.

[68] Y. Politi, R.A. Metzler, M. Abrecht, B. Gilbert, F.H. Wilt, I. Sagi, L. Addadi, S. Weiner, P. Gilbert, Transformation mechanism of amorphous calcium carbonate into calcite in the sea urchin larval spicule, PNAS. 105 (2008) 17362–17366, doi:10.1073/pnas.0806604105.

[69] M. Albéric, C.A. Stifler, Z. Zou, C.-Y. Sun, C.E. Killian, S. Valencia, M.-A. Mawass, L. Bertinetti, P.U.P.A. Gilbert, Y. Politi, Growth and regrowth of adult sea urchin spines involve hydrated and anhydrous amorphous calcium carbonate precursors, J. Struct. Biol. X 1 (2019) 100004, doi:10.1016/j.yjsbx.2019.100004.

[70] L.B. Gower, D.J. Odon, Deposition of calcium carbonate films by a polymer-induced liquid-precursor (PILP) process, J. Cryst. Growth 210 (2000) 719–734.

[71] Y. Politi, J. Mahamid, H. Goldberg, S. Weiner, L. Addadi, Asprich mollusk shell protein: in vitro experiments aimed at elucidating function in CaCO3 crystallization, CrystEngComm 9 (2007) 1171–1177, doi:10.1039/B709749B.

[72] H. Nakahara, G. Bevelander, The formation and growth of the prismatic layer ofPinctada radiata, Calc, Tis. Res. 7 (1971) 31–45, doi:10.1007/BF02062591.

[73] A.G. Checa, A.B. Rodríguez-Navarro, F.J. Esteban-Delgado, The nature and formation of calcitic columnar prismatic shell layers in pteriomorphian bivalves, Biomaterials 26 (2005) 6404–6414, doi:10.1016/j.biomaterials.2005.04.016.

[74] F. Nudelman, B.A. Gotliv, L. Addadi, S. Weiner, Mollusk shell formation: mapping the distribution of organic matrix components underlying a single aragonitic tablet in nacre, J. Struct. Biol. 153 (2006) 176–187, doi:10.1016/j.jsb.2005.09.009.

[75] B. Farre, A. Brunelle, O. Laprévote, J.-P. Cuif, C.T. Williams, Y. Dauphin, Shell layers of the black-lip pearl oyster Pinctada margaritifera: matching microstructure and composition, Comparative Biochem. Physiol. B. 159 (2011) 131–139, doi:10.1016/j.cbpb.2011.03.001.

[76] B. Pokroy, A.N. Fitch, F. Marin, M. Kapon, N. Adir, E. Zolotoyabko, Anisotropic lattice distortions in biogenic calcite induced by intra-crystalline organic molecules, J. Struct. Biol. 155 (2006) 96–103.

[77] E. Seknazi, B. Pokroy, Residual Strain and Stress in Biocrystals, Adv. Mater. Weinheim. 30 (2018) e1707263, doi:10.1002/adma.201707263.